51st AIAA/ASME/ASCE/AHS/ASC Structures, Structural Dynamics, and Materials Conference
 18th
12 - 15 April 2010, Orlando, Florida

AIAA 2010-2994

Hysteresis Characterization in Piezoceramic Stack Actuators and Its Influence on Vibration and Noise Reduction in Helicopters Using Actively Controlled Flaps

Eric R. Muir*, Li Liu†, Peretz P. Friedmann‡, Devesh Kumar§

Department of Aerospace Engineering, The University of Michigan, Ann Arbor, MI, 48109, USA

In this study, a characterization of hysteresis in a piezoceramic stack actuator similar to those employed in an actively controlled flap (ACF) system is performed to assess the effects of hysteresis on system performance. The effect of unmodeled actuation hysteresis may significantly reduce vibration and noise reduction capabilities. A hysteresis model based on the classical Preisach model has been developed from experimental data. The model displays good agreement with experimental data for input frequencies typical of those used for vibration and noise reduction in full-scale rotors. The hysteresis model has been incorporated into the Active Vibration and Noise Reduction (AVINOR) code, developed at the University of Michigan, so as to evaluate the effect of piezoceramic actuator hysteresis on vibration and noise reduction. The incorporation of hysteresis does not produce a significant performance degradation of the ACF system for vibration reduction at blade-vortex interaction (BVI) and dynamic stall conditions. For BVI noise reduction, hysteresis produces significant differences in flap deflection time histories, demonstrating the importance of hysteresis modeling. However, the overall noise reduction performance of the ACF system is not significantly affected.

Nomenclature

c	Blade chord
c_c	Control surface chord
C_W	Helicopter weight coefficient
$\mathbf{D}$	Matrix defined to be $\mathbf{T}^{\mathrm{T}}\mathbf{Q}\mathbf{T}+\mathbf{R}$
$f(t)$	Static hysteresis actuator output
f^-	Negative saturation output value
$F_{HX4}, F_{HY4}, F_{HZ4}$	Non-dimensional 4/rev hub shears
$J(\mathbf{z}_k, \mathbf{u}_k)$	Objective function
k	Control update index
L_b	Blade length
L_c	Control surface length
$M_{HX4}, M_{HY4}, M_{HZ4}$	Non-dimensional 4/rev hub moments
$\mathbf{M}$	Time-ordered sequence of maximum input values
$\mathbf{m}$	Time-ordered sequence of minimum input values
$\mathbf{M}_k$	Maximum input values
$\mathbf{m}_k$	Minimum input values

*Graduate Student Researcher, Student Member AIAA
†Postdoctoral Researcher, Member AIAA
‡François-Xavier Bagnoud Professor, Fellow AIAA
§Ph.D. Candidate

N	Number of flap deflection input harmonic
n	Number of trapezoid subdivisions of $S^+(t)$
N_b	Number of rotor blades
$\mathbf{Q}$	Weighting matrix for objectives to be reduced
$\mathbf{R}$	Weighting matrix on control input
R	Rotor radius
$S^+(t)$	Set of switched "up" hysteresis operators
$S^-(t)$	Set of switched "down" hysteresis operators
$\mathbf{T}$	Sensitivity, transfer matrix between control inputs and objective function
T	Limiting triangle
$\mathbf{u}_k$	Control input vector, k^{th} control step
$\mathbf{u}_{k,\text{opt}}$	Optimum value of control input vector
$u(t)$	Actuator input
x_c	Spanwise location of center of control surface
$\mathbf{z}_k$	Objective vector, k^{th} control step
α	Hysteresis operator switching "up" value
α_0	Maximum excitation value
β	Hysteresis operator switching "down" value
β_0	Minimum excitation value
β_p	Blade precone angle
δ	Flap deflection angle
δ_{Nc}, δ_{Ns}	N/rev cosine and sine amplitude of δ, respectively
$\hat{\gamma}_{\alpha\beta}$	Hysteresis operator
μ	Helicopter advance ratio
$\mu(\alpha, \beta)$	Hysteresis weight function
Ω	Rotor angular speed
ω_F, ω_L, ω_T	Rotating flap, lead-lag and torsional frequencies
ψ	Rotor azimuth angle
σ	Rotor solidity
θ_{FP}	Flight path angle
θ_{tw}	Built-in twist angle

I. Introduction

VIBRATION is one of the most critical concerns in the design of modern rotorcraft. Similarly, the generation of noise places an important constraint on helicopter design and operation. Stricter demands for enhanced performance, comfort, and customer acceptance in modern helicopters require designs with reduced vibration levels and noise signatures. In helicopters, the dominant source of vibrations is the rotor, from which vibrations are transferred to the rotor hub. The vibratory hub shear and moments in the fixed system occur at the blade passage frequency N_b/rev, where N_b is the number of blades in the rotor. Many methods, both passive and active, have been explored for vibration and noise reduction. The actively controlled partial-span trailing edge flap (ACF), shown in Figure 1(a) has emerged as a leading candidate for implementing on-blade active control for vibration reduction throughout the entire flight envelope.[1–3]

Piezoceramic stack actuators have proven themselves as an effective means for actuation of actively controlled partial-span trailing edge flaps. Piezoceramic actuators produce a one-dimensional displacement in response to an input voltage, which is suitable for ACF actuation. Furthermore, piezoceramic stack actuators are light, compact, exhibit fast frequency response, and thus possess high actuation bandwidth; they also require only small amounts of power for operation.[4] Combined with mechanical amplification mechanisms for enhancing the actuation stroke, piezoceramic stack actuators have been used successfully for vibration reduction in full scale rotors.[2,3] Figure 1(b) provides a schematic of an actuator-driven ACF on a BK 117 helicopter that has been flight tested by Eurocopter.[3]

During the last four years, two such actively controlled partial-span trailing edge flap systems have undergone full scale testing. In a joint Boeing/NASA/DARPA project, a full scale MD 900 bearingless ACF rotor was tested on a whirl tower in 2004, and subsequently, it was tested in both open loop and closed loop modes over the entire range of advance ratios in the 40 ft. X 80 ft. wind tunnel at NASA Ames Research

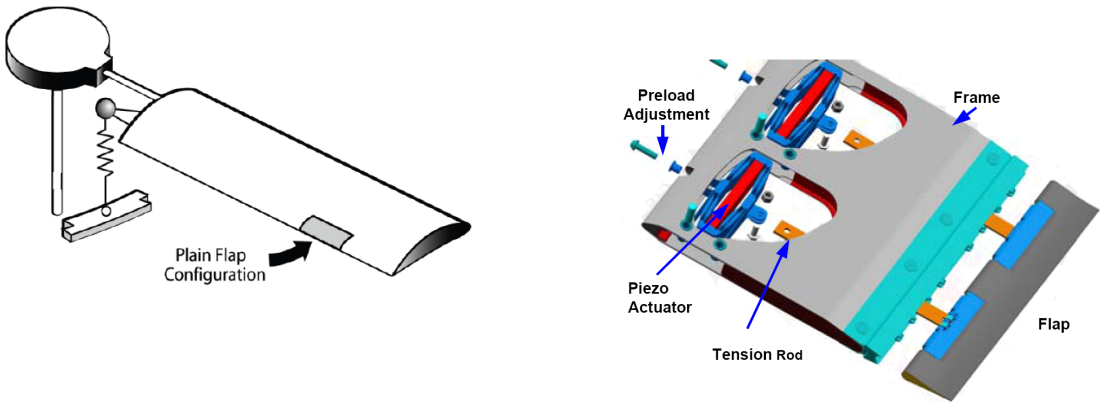

(a) Actively Controlled Trailing Edge Flap

(b) Eurocopter ACF[3]

Figure 1. Actively Controlled Flaps Utilizing Piezoceramic Actuators

Center in February-April 2008.[2] Starting in 2005, Eurocopter Germany has also been conducting flight tests on a hingeless four bladed rotor equipped with a three flap ACF system on a BK 117 helicopter.[3] These wind tunnel and flight tests have demonstrated in a definitive manner the potential of the ACF system to reduce vibration at both low and high speeds of forward flight. The potential of the ACF for reducing noise due to blade-vortex interaction (BVI) was also demonstrated. In these tests, vibration reduction in excess of 90% was obtained, accompanied by 5 db of noise reduction.[2,3] These tests also indicated that the nonlinear hysteresis characteristic of piezoceramic actuators may be sufficiently important that this effect should be accounted for in the modeling of the ACF system and its control law.

Hysteresis can be defined as an input voltage/output displacement nonlinearity that is influenced by previous excitation history. Experiments have also shown that hysteretic effects may not only be influenced by past excitation, but can also be affected by the time rate of change of excitation.[5] Thus, hysteresis can be categorized into two subsets: static (rate-independent) and dynamic (rate-dependent) hysteresis.[6,7] Static hysteresis describes hysteretic behavior where the input/output relationship is not sensitive to input rates. Conversely, dynamic hysteresis describes hysteretic behavior where the input/output relationship is sensitive to input rates. In the case of ACF for vibration and noise reduction in rotorcraft, studies have shown that flap deflection frequencies necessary to reduce hub loads, vibration, and noise are typically 2, 3, 4, and 5/rev for a 4 bladed rotor.[5,8] These correspond to voltage input frequencies of 10 to 50Hz for a typical rotorcraft. Thus, the influence of input rate should be examined for the application of piezoceramic stack actuators in ACF systems.

Bench tests performed on a piezoceramic stack actuator by Ganguli, Rao, and Viswamurthy suggested that input frequency significantly affects hysteresis; however, the results of these tests were limited to frequencies up to 20Hz.[5] Bench tests at higher frequencies were also performed on a piezoceramic stack actuator for frequencies up to 100Hz and, similarly, a significant influence of input frequency on hysteresis was noted.[9] Hu and Mrad tested a piezoceramic actuator at frequencies up to 800Hz and experienced a lesser influence of input frequency on hysteresis.[10] While the results of these tests suggest that hysteresis of piezoceramic stack actuators is dependent on input frequencies, it is unclear whether the experimental equipment/set-up used in these tests may have contributed to the hysteretic effects at high frequencies. Furthermore, the actuators used in some of these bench tests were not quite representative of an actuator suitable for implementation into an ACF system. Thus, the characterization of hysteresis for such actuators needs to be carefully re-examined.

The overall objectives of this paper are to conduct a combined experimental and numerical study of the hysteresis characteristics of an off-the-shelf piezoceramic stack actuator suitable for controlling an ACF system. In the experimental tests, the accuracy of measurement instrumentation is emphasized as to rule out contributions to hysteresis as a result of measurement errors. The hysteresis model resulting from this study is incorporated in the Active Vibration and Noise Reduction (AVINOR) aeroelatic simulation code so as to evaluate the effect of actuator hysteresis on vibration and noise reduction.[11] The specific objectives of this paper are:

1. Describe a mathematical model for simulating the hysteresis properties of a typical piezoceramic stack actuator.

2. Describe the bench tests performed for an off-the-shelf piezoceramic stack actuator, and present the experimental data and resulting hysteresis model of the piezoceramic actuator.

3. Incorporate the hysteresis model into the AVINOR code, perform simulations of the effect of hysteresis on vibration and noise reduction, and assess its impact on control law design.

II. Classical Preisach Model of Hysteresis

The Classical Preisach Model (CPM) is a mathematical model of static hysteresis originally developed to model hysteresis in ferromagnetic materials.[6] Subsequently, it has been successfully used to model a variety of systems exhibiting hysteresis, including piezoceramic material systems and piezoceramic stack actuators.[2, 5, 9, 10, 12]

A. Mathematical Description

The basis for the Classical Preisach Model is a continuous summation of two-way relays, which either takes value 1 or -1. Each relay, denoted by $\hat{\gamma}_{\alpha\beta}u(t)$, can be represented by a basic rectangular hysteresis loop with α denoting the switching "up" value and β denoting the switching "down" value such that α is greater than β, as shown in Figure 2(a). As the input is monotonically increased, the *abcde* branch is followed; as the input is then monotonically decreased, the *edfba* branch is followed. Notice that $\hat{\gamma}_{\alpha\beta}$ does not switch "up" until the input increases to α, and $\hat{\gamma}_{\alpha\beta}$ does not switch "down" until the input decreases to β.

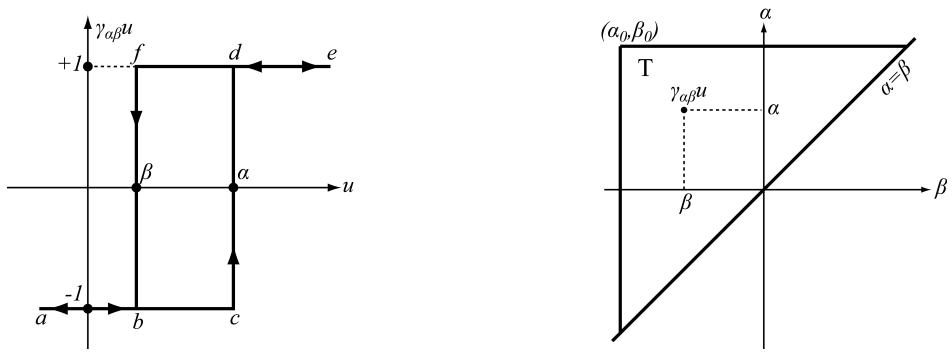

(a) Hysteresis Relay[6]

(b) Limiting Triangle T[6]

Figure 2. CPM Geometric Interpretation

Each relay value (1 or -1) is multiplied by its associated weight function and the integration of these products yields the output. The Classical Preisach Model can be mathematically expressed by Equation (1) [6, p. 3]:

$$f(t) = \int\int_{\alpha\geq\beta} \mu(\alpha,\beta)\hat{\gamma}_{\alpha\beta}u(t)d\alpha\, d\beta \tag{1}$$

Further analysis of the CPM is best accomplished through a geometric interpretation of the model, as suggested in Ref. 6. This geometric interpretation relies on the limiting triangle T, shown in Figure 2(b), defined with the hypotenuse on the line $\alpha \geq \beta$ and vertex equal to (α_0, β_0), the maximum and minimum excitation values, respectively. Each point within the triangle can be identified with only one particular relay whose switching values are equal to the point's particular α and β coordinates. Thus, the limiting triangle defines the integration area in Equation (1). The excitation history determines which relays are switched "on" and which relays are switched "off" forming two subsets within T; a set of relays that are switched "up" and a set of relays that are switched "down". The area of switched "up" relays is denoted by S^+, and the area of switched "down" relays is denoted by S^-. Figure 3(b) shows T divided into S^+ and S^- for an alternating input sequence of $u_1, u_2, \ldots, u_7$ as shown in Figure 3(a). An important characteristic of the

CPM is that only past input extrema affect the integration area and have an impact on the output response. The time-ordered sets of maximum and minimum values of input extrema are denoted by $\{M\}$ and $\{m\}$, respectively. In the case of the input sequence of u_1, u_2, ..., u_7, shown in Figure 3(a), $\{M\} = \{u_1, u_3, u_5, u_7\}$ and $\{m\} = \{u_2, u_4, u_6\}$.

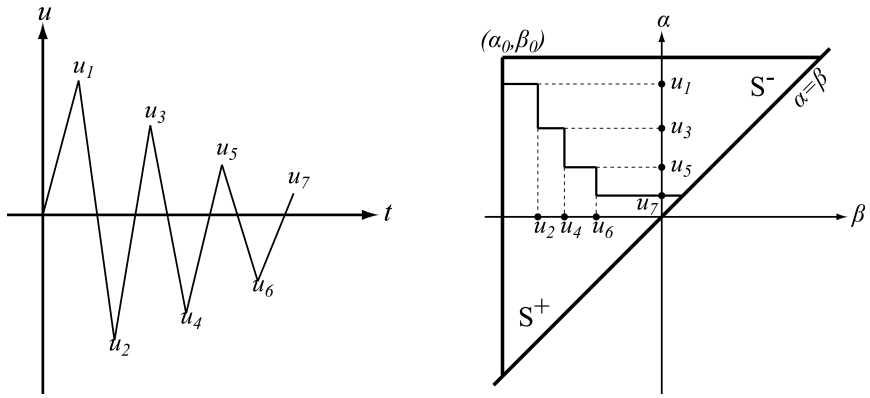

(a) Sample Alternating Input[6] (b) T For Sample Alternating Input[6]

Figure 3. CPM Dependence on Past Input Extrema

This CPM only considers the influence of past excitation history and does not accommodate for the influence of input/output rate. As mentioned previously, bench tests by Ganguli, Rao, and Viswamurthy suggest that hysteresis of a piezoceramic actuator varies significantly at higher input/output rates (frequencies). However, bench testing of our piezoceramic stack actuator, presented later in this paper, does not show a hysteresis dependence on input/output rate. Thus, a dynamic hysteresis model was not pursued in the current study.

B. Numerical Implementation

Numerical implementation of the hysteresis model given by Equation (1) requires the determination of a weight function value for each hysteresis operator. For experimental implementation, this approach requires differentiation of experimentally obtained data, which can magnify errors and noise inherent in the experimental data.[6,12] Instead, the geometric interpretation described previously is utilized in combination with a set of first-order transition curves obtained from experimental data. First-order transition curves result from a monotonically increasing input from the negative saturation value to some value α followed by a monotonic decrease to some value β, as shown in Figure 4. The output resulting from a first-order transisiton curve is denoted by $f_{\alpha\beta}$, where α is the "increase to" value and β is the "decrease to" value.

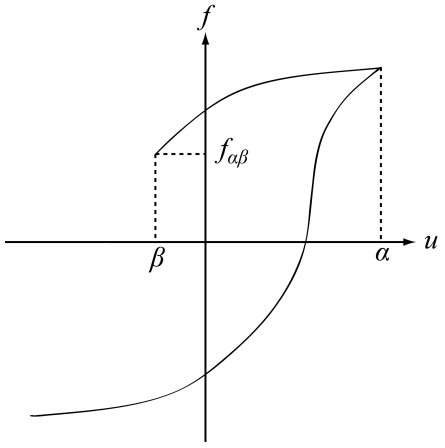

Figure 4. First-Order Transition Curve[6]

Further manipulations of the previous geometric interpretation and first-order transition curves yield the hysteresis output given by Equation (2), see Refs. 6,12. Equation (2) relies only on the output of first-order transition curves for the alternating series of input extrema, which implies that the time-ordered extrema sets, **M** and **m**, determine the "increase to" and "decrease to" value for each first-order transition curve output term in Equation (2). Thus, the CPM only requires experimentally obtained first-order transition curves and the alternating series of input extrema to determine the hysteresis output.

$$f(t) = f^{-} + \sum_{k=1}^{n} [f_{\mathbf{M}_k \mathbf{m}_k} - f_{\mathbf{M}_k \mathbf{m}_{k-1}}] \tag{2}$$

Equation (2) can be used directly with experimental data to determine the hysteresis behavior of the piezoceramic stack actuator output. Using a given input history and the current input value, the alternating series of input extrema can be determined. Then, triangle T can be divided into a mesh grid and each output value $f_{\alpha\beta}$ can be determined from experimentally obtained first-order transition curves. Interpolation of this data can be used to determine values of $f_{\alpha\beta}$ not explicitly found from experimental data. A computer code has been developed to implement this procedure for any given input waveform and experimentally obtained first-order transition curves.

III. Experimental Set-up

A CEDRAT APA900M piezoceramic stack actuator, shown in Figure 5(a), was tested in the Active Aeroelasticity and Structures Research Laboratory (AASRL) at the University of Michigan, courtesy of Professor Carlos Cesnik. This actuator was selected because its characteristics are representative of an actuator suitable for future use in a mach-scaled ACF system currently under development at the AASRL. Figure 5(b) shows the configuration of the experimental set-up. The actuator was tested in an unloaded, fixed-free configuration and a loaded, fixed-blocked configuration, as shown in Figures 5(c) and 5(d), respectively.

A large brass bracket was fabricated to fasten tightly to the optical table surface and to the piezoceramic stack actuator to prevent vibration in the mounting system. The brass bracket was also sized to weigh significantly more than the piezoceramic stack actuator so as to limit the amplitude of any vibration transfered from the actuator. When actuated at 50Hz sinusoidal input, with peak-to-peak voltage of 170V, the measured velocity of the brass bracket was less than 5μm/s. Furthermore, the electrical wires of the actuator were isolated to prevent vibrations from influencing the experimental data. For the fixed-blocked configuration, a cantilevered aluminum beam with stiffness 4.78N/mm was attached to the free-end of the actuator to investigate the effects of loading on the hysteresis characteristics of the actuator. The stiffness of the cantilevered beam was chosen to ensure nearly one-dimensional deflection of the beam.

A Polytec PSV-400 scanning vibrometer was used to obtain the velocity response of the unfixed-end of the actuator. The PSV-400 includes a sensor head to measure velocity, an input voltage signal generator, and data acquisition/management system. A key benefit of the PSV-400 is its ability to simultaneously acquire velocity and voltage data using the same data acquisition system providing essentially zero time delay between input voltage and output velocity measurements. The lack of time delay ensures that the measured hysteresis is solely due to the actuator response rather than phase lag present in the data acquisition system.

The input voltage was generated by the PSV-400 data management software and was amplified by a power amplifier with a gain factor of 200. The power amplifier was tested to ensure that it did not contribute any phase lag to the input signal through the use of a dual-channel oscilloscope. The PSV-400 sensor head was placed at an optimal distance from the actuator and special care was taken to properly align the sensor head. The resulting experimental setup accurately determined the input/output response of the actuator while avoiding the influence of external vibrations and displacements. The measured velocity data was filtered using MATLAB and integrated to yield the displacement response of the actuator.

IV. Brief Description of Aeroelastic Simulation Code

The mathematical model in AVINOR consists of several fairly complex ingredients which are combined into a sophisticated aeroelastic response and noise generation simulation that is used to demonstrate active vibration and noise reduction using single or dual ACF systems. The principal ingredients of this simulation

(a) CEDRAT APA900M piezoceramic stack actuator

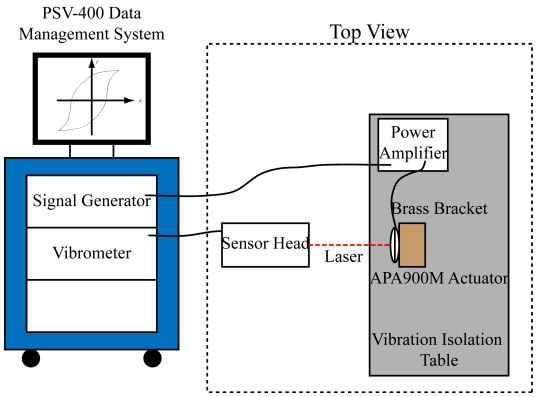

(b) Schematic of experimental set-up

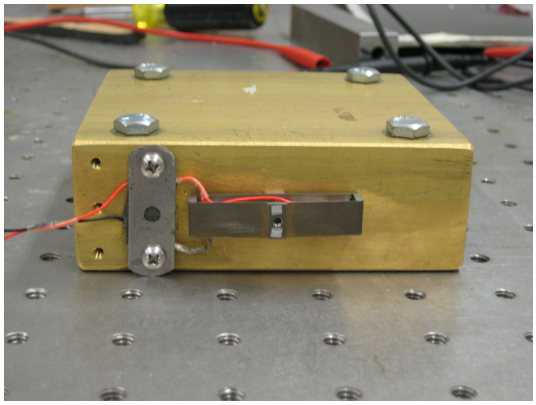

(c) Fixed-free experimental configuration

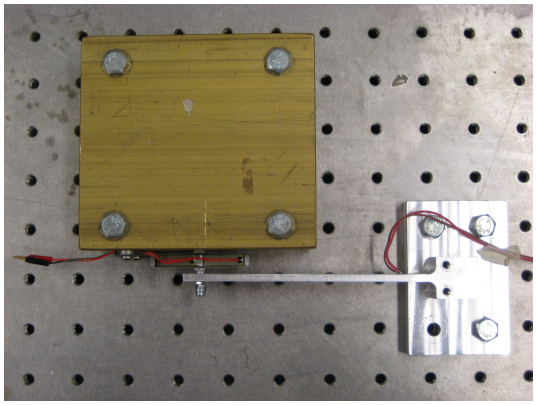

(d) Fixed-blocked experimental configuration

Figure 5. Experimental Set-up

are: (1) a structural dynamic model; (2) an aerodynamic model; (3) an acoustic model and (4) a coupled trim/aeroelastic solution procedure that generates the blade response. A controller based on the higher harmonic control (HHC) algorithm is subsequently used to conduct active vibration or noise control. The various ingredients of this model are described concisely below, and additional details can be found in Ref. 11.

A. Aerodynamic Model

The aerodynamic model consists of several important ingredients that are essential for a coupled aeroelastic/acoustic simulation. These are:

1. An unsteady compressible, two-dimensional aerodynamic model for the blade-flap combination that accounts for variations in the oncoming velocity. The model is based upon a rational function approximation (RFA) of the aerodynamic loads, Ref. 13, which produces aerodynamic cross-sectional loads (lift, moment, flap-hinge moment) in the time domain for either the blade or the blade-flap combination in attached flow. The RFA model used for the computation of the chordwise pressure distribution, Ref. 8, is an extension of the model that is required for the acoustic calculations.

2. An enhanced free wake model that provides the non-uniform inflow distribution at closely spaced azimuthal steps. The enhancements consist of improved wake resolution and refined modeling of the inboard wake structure, that are needed for accurate BVI noise calculations.[14]

3. The ONERA dynamic stall model is used to model the two dimensional unsteady loads in separated flow.

B. Structural Model

The configuration considered in this present study represents a four-bladed hingeless rotor that resembles an MBB BO-105 rotor. Each blade has a root offset e, and it rotates with constant angular speed Ω, and has fully-coupled flap, lead-lag, and torsional dynamics including nonlinearities due to moderate blade deflections. The equations of motion are discretized using the global Galerkin method, based upon the free vibration modes of the rotating blade. Three flapping modes, two lead-lag modes and two torsional modes are used in the actual implementation.

C. Acoustic Model

The acoustic analysis is based on a modified version of the WOPWOP[15] code which computes helicopter noise using the Ffowcs-Williams Hawkings equation with the quadrupole term neglected. The WOPWOP code was modified so that it is based on a fully flexible blade model that is consistent with the structural dynamic model.[8] The input into the acoustic code is the unsteady pressure distribution on the surface of the blade that is calculated from a combination of the RFA unsteady aerodynamic model which yields chordwise and spanwise pressure distributions that also depend on the non-uniform inflow provided by the free-wake model.

D. Solution Procedure

The combined structural and aerodynamic equations form a system of coupled differential equations that can be cast in state variable form. They are then integrated in the time domain using the Adams-Bashforth DE/STEP predictor-corrector algorithm. Two types of trim procedures can be implemented, including a propulsive trim where six equilibrium equations (three forces and three moments) are enforced, as well as a wind tunnel trim where zero pitch and moment conditions are enforced. These trim equations are solved in a coupled manner with the aeroelastic equations of motion. Hub vibratory loads are obtained by integrating the distributed aerodynamic and inertial loads over the blades, transforming to the hub fixed system, and adding the contribution of the various blades. The BVI noise is computed by the acoustic module using the unsteady distributed aerodynamic pressure and blade response which are obtained after the coupled trim/aeroelastic calculation is completed.

E. Control Algorithm

The higher-harmonic control algorithm is used for both noise and vibration reduction. The stability, robustness, and convergence properties of this algorithm were discussed in detail in Ref. 16. The algorithm is based on a linear, quasi-static, frequency domain representation of helicopter response to control inputs. The inputs to the algorithm are comprised of a combination of flap deflection harmonics with discrete frequencies of $N_{\min}$-$N_{\max}$/rev. The total flap deflection is given as

$$\delta(\psi) = \sum_{N=N_{\min}}^{N_{\max}} [\delta_{Nc}\cos(N\psi) + \delta_{Ns}\sin(N\psi)] \tag{3}$$

The lowest component of higher harmonic frequency input has been typically chosen to be 2/rev. The choice of $N_{\max}$ is based on the number of the blades, since the dominant vibrations at the hub are N_b/rev; typically $N_{\max} = 5$ for a four-bladed rotor. These pitch deflections are related to the vibration or noise level magnitudes through a transfer matrix $\mathbf{T}$, given by:

$$\mathbf{T} = \frac{\partial \mathbf{z}_k}{\partial \mathbf{u}_k}. \tag{4}$$

The control strategy is based on the minimization of a performance index that was originally developed for vibration reduction, which is a quadratic function of the quantities that are being reduced (vibration or noise) $\mathbf{z}_k$ and control input amplitudes $\mathbf{u}_k$:

$$J(\mathbf{z}_k, \mathbf{u}_k) = \mathbf{z}_k^{\mathrm{T}}\mathbf{Q}\mathbf{z}_k + \mathbf{u}_k^{\mathrm{T}}\mathbf{R}\mathbf{u}_k, \tag{5}$$

The subscript k refers to the k^{th} control step, reflecting the discrete-time nature of the control. The time interval between each control step must be sufficient to allow the system to return to the steady state,

typically in 3–5 revolutions, so that the vibration or noise levels can be accurately measured. The optimal control law is given by:

$$\mathbf{u}_{k,\text{opt}} = -\mathbf{D}^{-1}\mathbf{T}^{\mathrm{T}}\mathbf{Q}\{\mathbf{z}_0 - \mathbf{T}\mathbf{u}_0\} \tag{6}$$

where

$$\mathbf{D} = \mathbf{T}^{\mathrm{T}}\mathbf{Q}\mathbf{T} + \mathbf{R} \tag{7}$$

For vibration reduction studies, the vector $\mathbf{z}_k$ consists of N_b/rev vibration levels as represented by hub shears and moments. For noise reduction the objective vector $\mathbf{z}_k$ consists of harmonic components of BVI noise, measured by a skid-mounted feedback microphone which provides good correlation with ground-based noise levels.[14] Furthermore, an adaptive version of the HHC algorithm was used in the noise reduction studies, which has been shown to be advantageous for noise control.[14] In the adaptive variant, the transfer matrix $\mathbf{T}$ is identified online, using a recursive least-squares technique, following the method described in Ref. 16.

F. Incorporation of Hysteresis Model into the AVINOR Code

The hysteresis model developed earlier was incorporated into the AVINOR code to account for hysteresis between the actuator input and the flap deflection output. The HHC controller, described previously, determines the desired multi-harmonic flap deflection as a function of azimuthal angle for a given flight condition. The desired input in flap deflection angle is first converted to actuator input in voltage, assuming a linear relationship, where the flap deflection extrema (set at $\pm 4^\circ$ in this study) correspond to the actuator input extrema. The actuator displacement is then obtained by the hysteresis model which relates the input voltage to the output displacement. The displacement is subsequently converted back to flap deflection assuming linear amplification. Since the hysteretic characteristics of the piezoceramic stack actuator tested in this study are insensitive to input rate for the practical range of flap deflection frequencies, the hysteresis model obtained at one frequency (30Hz) is used in AVINOR for all simulations.

V. Results and Discussions

The experimental results from input/output tests of the CEDRAT APA900M actuator, including the fixed-free and fixed-blocked configurations, are presented first. The hysteresis models developed from the experimental results are compared to measurements. Subsequently, aeroelastic simulations are conducted with the hysteresis model implemented in AVINOR, in order to examine the effects of hysteresis on vibration and noise reduction characteristics of the active flap system.

A. Fixed-Free Experimental Results

The piezoceramic stack actuator was initially tested with 1Hz sinusoidal inputs and 1Hz triangular inputs with peak-to-peak voltages (Vppk) ranging from 5Vppk to 170Vppk. The resulting velocity data was filtered, integrated, and processed to determine the first-order transition curve outputs needed for implementation of the CPM. The results from these tests closely match the input/output data supplied by the manufacturer for a 5Hz sinusoid, shown in Figure 6, confirming the accuracy of the experimental set-up and data collection system. In addition, the sinusoidal and triangular inputs had very similar output results, indicating that the form of the input waveform at low frequencies has negligible effect on the actuator response.

The 1Hz hysteresis model results were compared to the measured output displacements for an arbitrary input composed of 2, 3, 4, and 5Hz sinusoid waves. Figure 7(a) shows that the 1Hz hysteresis model results correlated well with the experimental data obtained for this input. The model was also compared to experimental data for inputs representative of those determined by the AVINOR code for vibration and noise reduction caused by blade vortex interaction, for a rotor speed of 60 RPM. While 60 RPM is an unrealistic rotor speed for a full-scale rotor, it was chosen so that the vibration and noise reduction inputs determined by the AVINOR code would contain harmonics in the range of 2-5Hz. Figures 7(b)- 7(c) show the 1Hz hysteresis model results and experimental data for vibration reduction and noise reduction inputs, respectively. Once again, the 1Hz hysteresis model results showed good agreement with the experimental data.

Tests were also performed at 30Hz and 50Hz sinusoidal inputs with voltages ranging from 5Vppk to 170Vppk. A hysteresis model was developed using the experimental data from these tests. Figure 8 shows an input/output hysteresis plot for 1Hz, 30Hz, and 50Hz sinusoidal inputs with a voltage of 170Vppk. The

results shown in Figure 8 suggest that input frequencies up to 50Hz have negligible influence on the hysteresis characteristic of our actuator. Therefore, the development of a dynamic hysteresis model was not pursued.

The 30Hz hysteresis model was also compared to experimental data for inputs representative of those determined by the AVINOR code for vibration and noise reduction for rotor speeds of 60 RPM and 300 RPM. A rotor speed of 300 RPM is representative of helicopter rotor speeds, and the vibration and noise reduction inputs contain harmonics in the range of 10-25Hz. Figure 9(a)- 9(d) show the 30Hz hysteresis model results and experimental data for vibration reduction and noise reduction inputs for both rotor speeds. The 30Hz hysteresis model showed equally good agreement with the experimental data for rotor speeds of both 60 RPM and 300 RPM. These results suggest that the 30Hz hysteresis model is capable of modeling hysteresis for input frequencies up to 30Hz.

Finally, the 50Hz hysteresis model was compared to experimental data for inputs representative of those determined by the AVINOR code for vibration and noise reduction for a rotor speeds of 420 RPM. A rotor speed of 420 RPM is also representative of helicopter rotor speeds, and the vibration and noise reduction inputs contain harmonics in the range of 14-35Hz. Figure 10(a)- 10(d) show the 50Hz hysteresis model results and experimental data for vibration reduction and noise reduction inputs for a 60 RPM rotor and a 420 RPM rotor speed. The 50Hz hysteresis model showed equally good agreement with the experimental data for a rotor speed of 60 RPM and 420 RPM and suggest that the 50Hz hysteresis model is capable of modeling hysteresis for input frequencies up to 50Hz.

Initial testing of the actuator with 135Vppk sinusoidal inputs up to 95Hz was also performed. Figure 11 provides a input/output hysteresis plot for this range of input frequencies. The increase in net displacement with increasing frequency is due to the input frequency approaching the resonance frequency of the actuator. As previously mentioned, the CEDRAT APA900M actuator was selected for potential future use in a mach-scaled ACF system requiring actuator inputs frequencies up to 120Hz requiring further characterization of this near-resonance response. However, for the case of the AVINOR simulations presented later in this paper, only actuator input frequencies up to 35Hz are required. Thus, the hysteresis models based on the 1Hz, 30Hz, and 50Hz input frequencies are sufficient, for the present study.

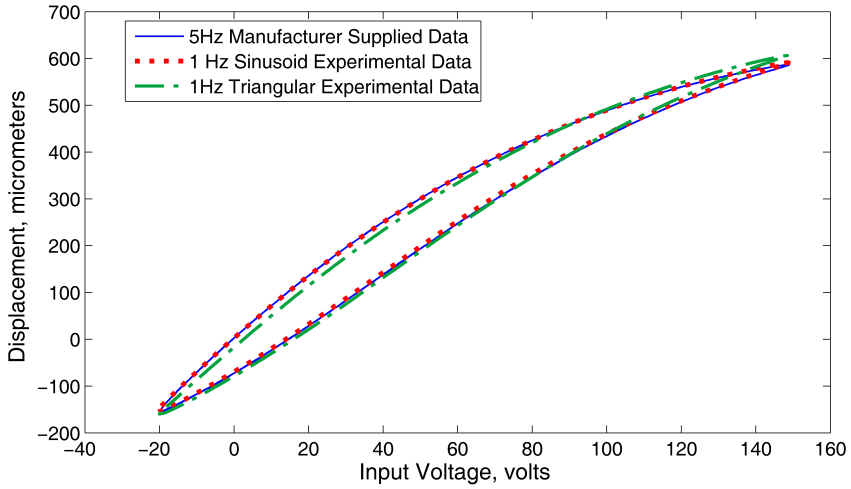

Figure 6. Comparison of manufacturer and experimental hysteresis curves

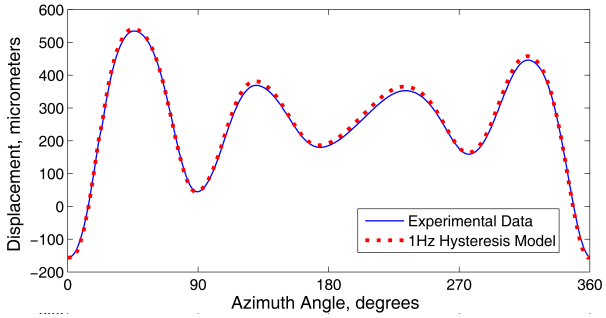

(a) Input waveform composed of 2-5Hz sinusoid components

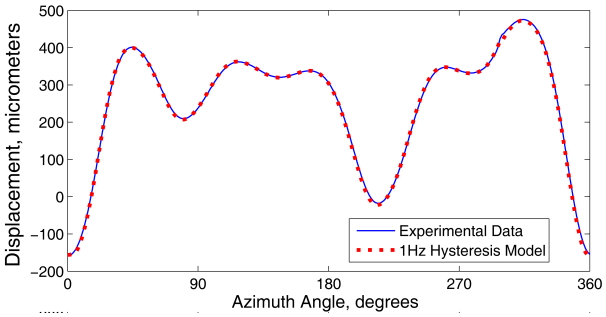

(b) Input waveform representative of that determined by AVINOR code for reduction of noise due to blade-vortex interaction for a rotor speed of 60 RPM

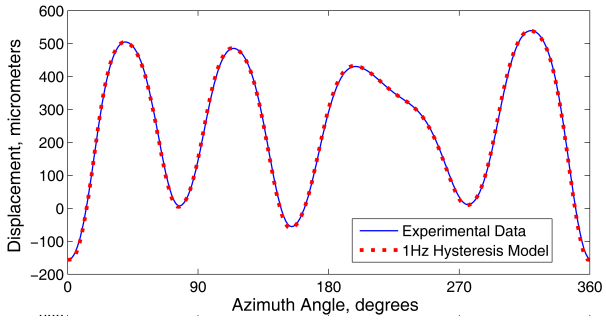

(c) Input waveform representative of that determined by AVINOR code for reduction of vibration due to blade-vortex interaction for a rotor speed of 60 RPM

Figure 7. Comparison of experimental data and 1Hz hysteresis model results

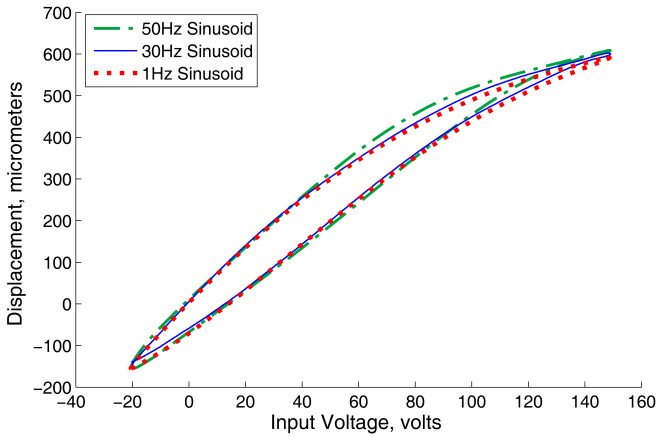

Figure 8. Actuator response for 1Hz, 30Hz, and 50Hz sinusoidal inputs with a voltage of 170Vppk

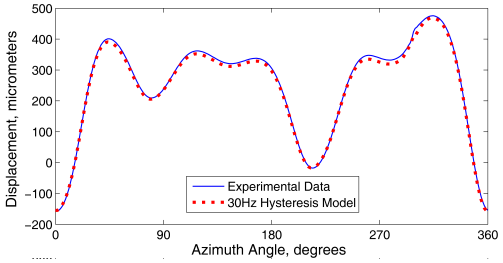

(a) Input waveform representative of that determined by AVINOR code for reduction of noise due to blade-vortex interaction for a rotor speed of 60 RPM

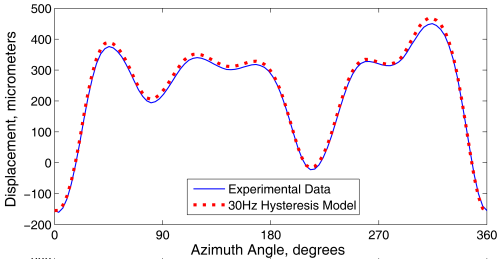

(b) Input waveform representative of that determined by AVINOR code for reduction of noise due to blade-vortex interaction for a rotor speed of 300 RPM

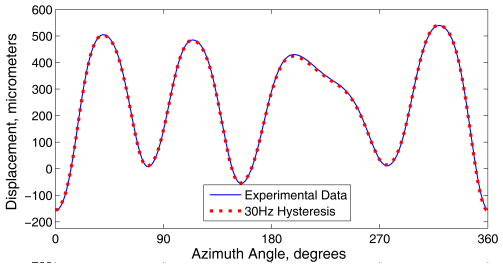

(c) Input waveform representative of that determined by AVINOR Code for reduction of vibration due to blade-vortex interaction for a rotor speed of 60 RPM

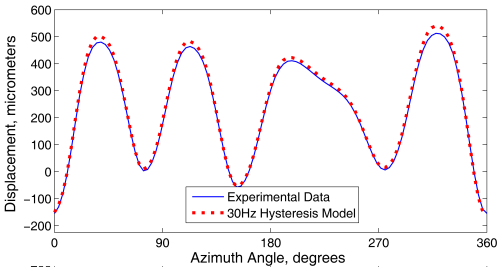

(d) Input waveform representative of that determined by AVINOR code for reduction of vibration due to blade-vortex interaction for a rotor speed of 300 RPM

Figure 9. Comparison of experimental data and 30Hz hysteresis model results

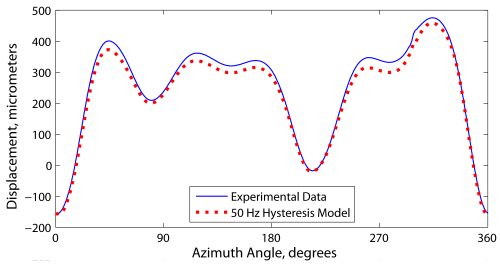

(a) Input waveform representative of that determined by AVINOR code for reduction of noise due to blade-vortex interaction for a rotor speed of 60 RPM

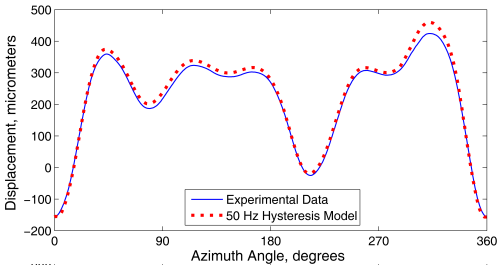

(b) Input waveform representative of that determined by AVINOR code for reduction of noise due to blade-vortex interaction for a rotor speed of 420 RPM

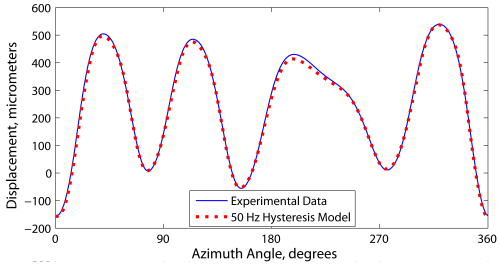

(c) Input waveform representative of that determined by AVINOR code for reduction of vibration due to blade-vortex interaction for a rotor speed of 60 RPM

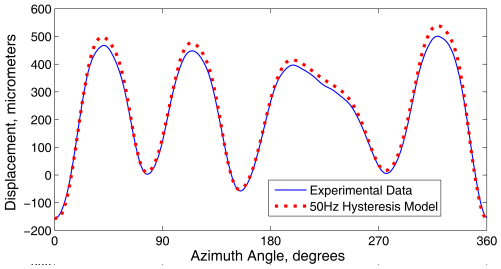

(d) Input waveform representative of that determined by AVINOR code for reduction of vibration due to blade-vortex interaction for a rotor speed of 420 RPM

Figure 10. Comparison of experimental data and 50Hz hysteresis model results

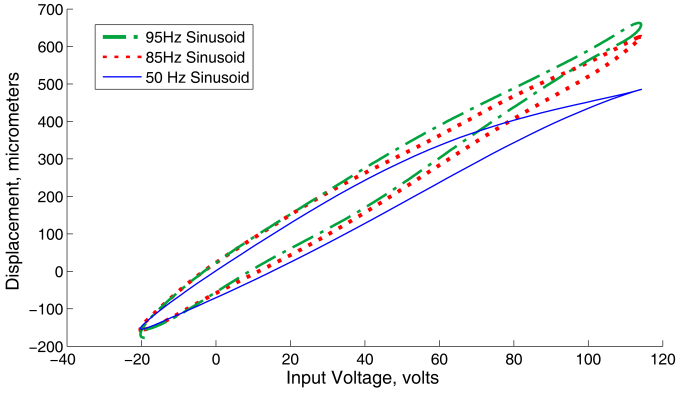

Figure 11. Actuator response for inputs up to 120Hz

B. Fixed-Blocked Experimental Results

In acknowledgment that an unloaded actuator is unrealistic due to the presence of aerodynamic loads on the trailing-edge flap, an investigation into the effects of load on the hysteresis characteristic of the CEDRAT APA900M actuator was also performed. The actuator was tested in a "fixed-blocked" configuration in which the free-end of the actuator was attached to a cantilevered aluminum beam of stiffness 4.78N/mm. Figure 12 provides the input/output hystersis plots for the fixed-blocked configuration as well as the fixed-free configuration for a sinusoidal input voltage of 135Vppk at 1Hz, 30Hz, and 50Hz. The results from this fixed-blocked test suggest that the displacement of the actuator for a given input voltage is proportional to the applied stiffness. Thus the presence of a stiffness simply "scales" the actuator output and thus the hysteresis curve; however, the width of the hysteresis curve remains proportional. Overall, the effects of trailing edge flap aerodynamic loading on the hysteresis characteristic of a piezoceramic actuator are significant in the selection of an appropriate actuator as the maximum net displacement is affected; however, the effect of loading on hysteresis is insignificant.

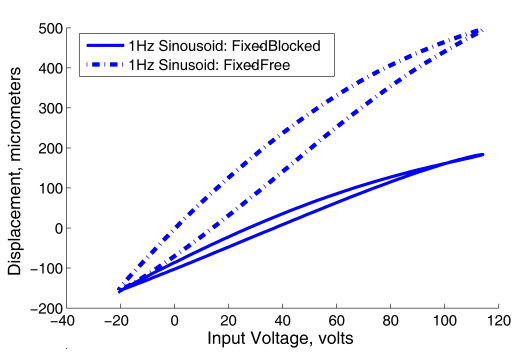

(a) 1Hz Fixed-Free and Fixed-Blocked Response

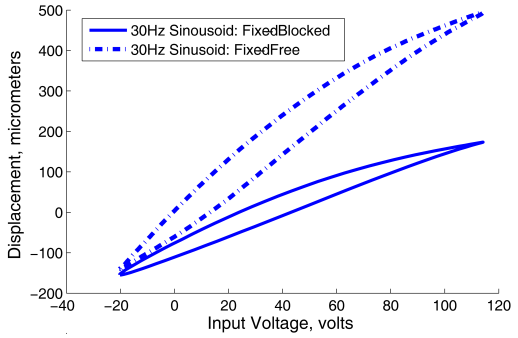

(b) 30Hz Fixed-Free and Fixed-Blocked Response

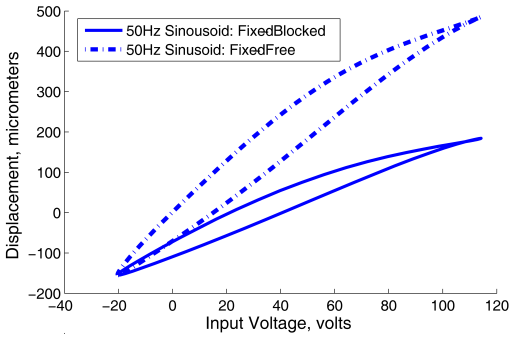

(c) 50Hz Fixed-Free and Fixed-Blocked Response

Figure 12. Actuator response for fixed-free and fixed-blocked configuration at 1Hz, 30Hz, and 50Hz

C. Vibration and Noise Reduction with Actuator Hysteresis

The results presented in this section are obtained for a four-bladed hingeless rotor configuration resembling the MBB BO-105. The properties of the helicopter configuration used in the computations are summarized in Table 1. The characteristics of the actively controlled flap configurations are given in Table 2, which is a single servo flap configuration. As mentioned earlier, a microphone is placed on the skid for noise feedback control, as illustrated in Fig. 13.

Two flight conditions are considered for vibration reduction studies: 1) low speed 6.5° descent at the advance ratio $\mu = 0.15$, where high vibratory loads are generated due to heavy BVI, and 2) high speed level flight at $\mu = 0.35$, where dynamic stall effects are responsible for high vibration levels. Simulations for noise reduction are conducted under BVI conditions only.

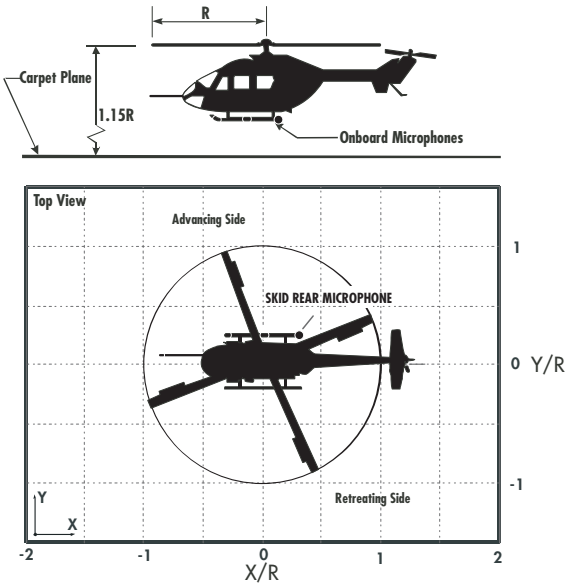

Figure 13. Microphone location on the helicopter skid for noise feedback.

Table 1. MBB BO-105 hingeless blade configuration.

Rotor Data	
$N_b = 4$	$c = 0.05498 L_b$
$\omega_F = 1.12, 3.41, 7.62$	$C_{do} = 0.01$
$\omega_L = 0.73, 4.46$	$C_{mo} = 0.0$
$\omega_T = 3.17$	$a_o = 2\pi$
$\theta_{\text{tw}} = -8^\circ$	$\theta_{\text{FP}} = 6.5^\circ$
$\gamma = 5.5$	$\sigma = 0.07$
$\beta_p = 2.5^\circ$	
Helicopter Data	
$C_W = 0.005$	$\mu = 0.15$ or 0.35
$L_b = 4.91\,\text{m}$	$\Omega = 425\,\text{RPM}$

Table 2. Flap configuration.

$c_c = 0.25c$	
Single Servo Flap	
$x_c = 0.75 L_b$	$L_c = 0.12 L_b$

1. Effect of hysteresis on vibration reduction at BVI and dynamic stall conditions

The baseline vibratory hub loads, as well as the controlled loads at BVI conditions, with and without actuator hysteresis effects, are shown first in Fig. 14. The active flap system is capable of producing approximately 80% reduction in the vibration objective at this flight condition, compared to the baseline. Incorporation of hysteresis in the aeroelastic code does not result in a significant degradation in the performance of the active flap system for vibration reduction, as is evident from Fig. 14. With hysteresis effects included, the controller produces 76% reduction in the vibration objective, slightly lower than the 81% reduction when hysteresis is neglected.

The flap deflection time histories during vibration reduction are depicted in Fig. 15. The deflections are shown for one rotor revolution, with maximum flap deflection of approximately 4°. There are only slight differences observed in the flap deflections due to hysteresis, as evident from Fig. 15.

Next, the significance of hysteresis during vibration reduction at a higher advance ratio of $\mu = 0.35$, where dynamic stall effects can be important, is examined in Fig. 16. Again, the actuator hysteresis does not affect the performance of the vibration controller under the dynamic stall condition. The flap deflections for this case are shown in Fig. 17. The HHC controller with hysteresis yields very similar flap deflections as those obtained without hysteresis, demonstrating the ability of the controller to perform well in the presence of actuator hysteresis.

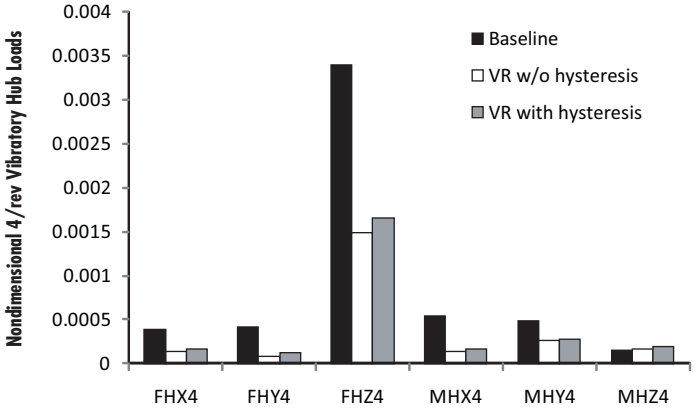

Figure 14. Vibratory hub loads for the baseline and vibration reduction with and without consideration of hysteresis; low speed descending flight case ($\mu = 0.15$, 6.5° descent angle).

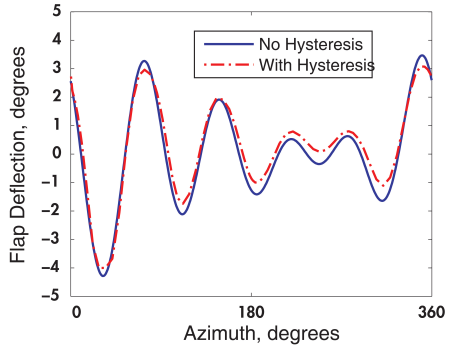

Figure 15. Flap deflection time histories for vibration reduction with and without consideration of hysteresis; low speed descending flight case ($\mu = 0.15$, 6.5° descent angle).

2. Effect of hysteresis on BVI noise reduction

Next, the performance of the active controller for noise reduction is further examined, so as to determine the effect of hysteresis on BVI noise reduction at the advance ratio of $\mu = 0.15$. Figure 18 shows the contour plots of BVI noise levels, in decibel, on a carpet plane located $1.15R$ below the hub plane, for the baseline case,

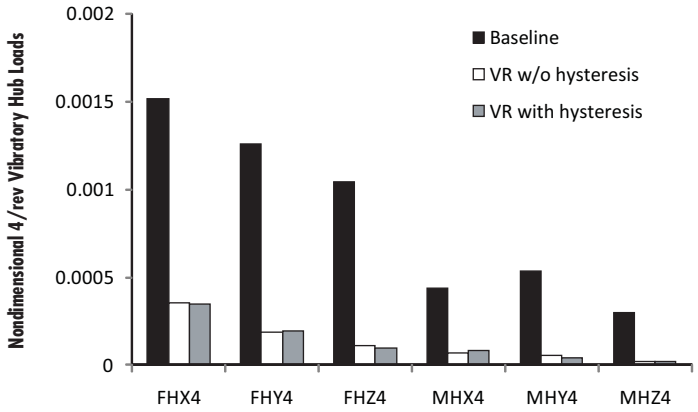

Figure 16. Vibratory hub loads for the baseline and vibration reduction with and without consideration of hysteresis; high speed forward flight case ($\mu = 0.35$, level flight).

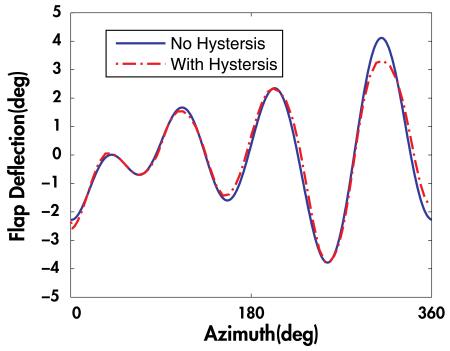

Figure 17. Flap deflection time histories for vibration reduction with and without consideration of hysteresis; high speed forward flight case ($\mu = 0.35$, level flight).

as well as noise reduction with and without hysteresis. The noise directivity of the baseline case (Fig. 18a) is characterized by the high noise levels on the advancing and retreating side. The noise levels on the carpet plane are reduced by 3-5dB by the controller without considering hysteresis, as can be seen from Fig. 18b. When the hysteresis is included (Fig. 18c), the noise controller produces similar reductions on the advancing side, while a slight 2dB increase is found on the retreating side.

Examining the flap deflection time histories shows that the two cases, with and without hysteresis, result in substantially different flap deflections, as shown in Fig. 19. The different flap deflections indicate that a different local optimum is found when the hysteresis model is included. This can be attributed to the stronger nonlinearity of BVI noise emission in response to flap inputs. Therefore, it is important to include the hysteresis effect when noise reduction is considered.

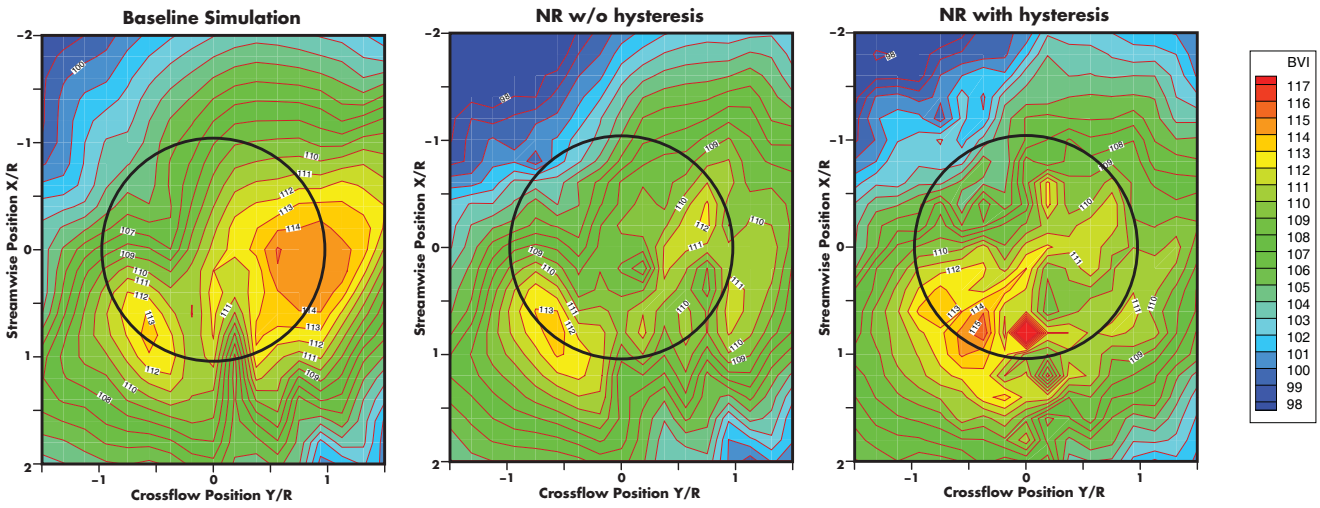

Figure 18. Comparison of BVI sound pressure levels on a carpet plane below rotor for the baseline and noise reduction with and without consideration of hysteresis; low speed descending flight case ($\mu = 0.15$, 6.5° descent angle).

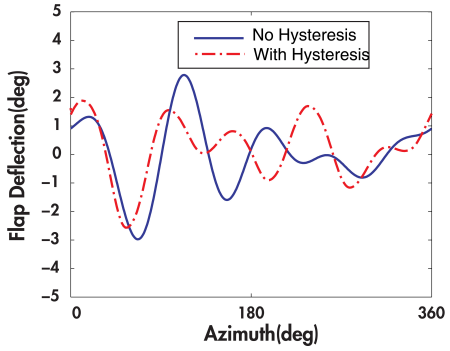

Figure 19. Flap deflection time histories for noise reduction with and without consideration of hysteresis; low speed descending flight case ($\mu = 0.15$, 6.5° descent angle).

VI. Concluding Remarks

Piezoceramic material systems have been successfully implemented to actuate actively controlled trailing edge flaps on rotorcraft blades for vibration and noise reduction. Piezoceramic stack actuators are prone to hysteresis behavior between their input voltage and output displacement. A CEDRAT APA900M piezoceramic stack actuator suitable for use in an ACF system has been tested in a fixed-free and fixed-blocked configuration for a number of input frequencies. The actuator was tested with a series of sinusoidal inputs

to obtain experimental data necessary to complete the hysteresis model. For frequencies up to 50Hz, the hysteresis model exhibits good agreement with experimental data for representative inputs for vibration and noise reduction and provides a good characterization of the piezoceramic stack actuator. Tests were also conducted for input frequencies up to 95Hz sinusoidal inputs and the results of these tests indicate that the hysteresis characteristic of our piezoceramic stack actuator is insensitive to higher inputs rates. Overall, the experimental results indicate that the hystersis characteristic of this actuator are not dependent on input frequency or influenced by the presence of a load force or stiffness and confirm the accuracy of our hysteresis model. This differs from earlier results published in Refs. 4 and 5.

Aeroelastic simulations of a four-bladed hingeless rotor configuration resembling the MBB BO-105 were conducted using the AVINOR code. In these simulations, the hysteresis model was included so as to assess its effects on vibration and noise reduction. As a result of these simulations, several conclusions can be drawn regarding the effect of hysteresis on vibration and noise reduction.

1. For the case of low-speed descending flight ($\mu = 0.15$, 6.5° descent angle), where BVI is a dominant source of vibrations, the incorporation of hysteresis demonstrated an insignificant effect on the vibration reduction performance of the ACF system. The HHC controller demonstrated the ability to compensate for the effect of hysteresis in vibration reduction under BVI conditions. Furthermore, the flap deflection history does not differ significantly between the cases with and without consideration of hysteresis, highlighting the insensitivity of the ACF system to hysteresis in vibration reduction.

2. For the case of high-speed forward flight ($\mu = 0.35$, level flight), where dynamic stall effects are important, the incorporation of hysteresis also indicated that its effect on the vibration reduction performance of the ACF system is not significant. Similar to the low speed case, the flap deflection history does not differ significantly between the cases with and without consideration of hysteresis.

3. For the case of noise reduction during low-speed descending flight ($\mu = 0.15$, 6.5° descent angle), the incorporation of hysteresis had a more noticeable effect on noise reduction due to the nonlinear nature of BVI noise control by the ACF system. While noise reduction on the advancing side is similar to the case of unmodeled hysteresis (3-5dB), the presence of hysteresis produced a significant difference in the flap deflection time history resulting from a different local optimum. The HHC controller also showed the ability to compensate for the presence of hysteresis in the noise reduction case. However, the significant difference in flap deflection histories indicates that the incorporation of hysteresis is important for the case of noise reduction under BVI conditions.

References

[1]Friedmann, P. P. and Millott, T. A., "Vibration Reduction in Rotorcraft Using Active Control: A Comparison of Various Approaches," *Journal of Guidance, Control, and Dynamics*, Vol. 18, No. 4, July-August 1995.

[2]Straub, F. K., Anand, V. R., Birchette, T. S., and Lau, B. H., "Wind Tunnel Test of the SMART Active Flap Rotor," *Proceedings of the 65th Annual AHS Forum*, Grapevine, TX, May 2009.

[3]Konstanzer, P. and Enenkl, B., "Recent Advances in Eurocopter's Passive and Active Vibration Control," *Proceedings of the 64th Annual AHS Forum*, Montreal, Canada, April-May 2008.

[4]Viswamurthy, S. R. and Ganguli, R., "Effect of Piezoelectric Hysteresis Nonlinearity on Helicopter Vibration Control Using Trailing Edge Flaps," *Proceedings of the 46th AIAA/ASME/ASCE/AHS/ASC Structures, Structural Dynamics, and Materials Conference*, Austin, TX, April 2005.

[5]Viswamurthy, S. R., Rao, A. K., and Ganguli, R., "Dynamic Hysteresis of Piezoceramic Stack Actuators Used in Helicopter Vibration Control: Experiments and Simulations," *Smart Materials and Structures*, Vol. 16, 2007, pp. 1109–1119.

[6]Mayergoyz, I. D., *Mathematical Models of Hysteresis and Their Applications*, Elsevier Science Inc, 2003.

[7]Mayergoyz, I. D., "Dynamic Preisach Models of Hysteresis," *IEEE Transactions on Magnetics*, Vol. 24, No. 6, July-August 1988, pp. 2925–2927.

[8]Patt, D., Liu, L., and Friedmann, P. P., "Rotorcraft Vibration Reduction and Noise Prediction Using a Unified Aeroelastic Response Simulation," *Journal of the American Helicopter Society*, Vol. 50, No. 1, January 2005, pp. 95–106.

[9]Yu, Y., Xiao, Z., Naganathan, N. G., and Dukkipati, R. V., "Dynamic Preisach Modeling of Hysteresis for the Piezcoceramic Actuator System," *Proceedings of the Institution of Mechanical Engineers*, Vol. 215, 2001, pp. 511–521.

[10]Hu, H. and Mrad, R. B., "On the classical Preisach Model for Hysteresis in Piezoceramic Actuators," *Mechatronics*, Vol. 13, 2003, pp. 83–94.

[11]Glaz, B., Friedmann, P. P., Liu, L., Kumar, D., and Cesnik, C. E. S., "The AVINOR Aeroelastic Simulation Code and its Application to Reduced Vibration Composite Rotor Blade Design," *Proceedings of the 50th AIAA/ASME/ASCE/AHS/ASC Structures, Structural Dynamics, and Materials Conference*, Palm Springs, CA, May 2009.

[12]Ge, P. and Jouaneh, M., "Modeling hysteresis in Piezoceramic Actuators," *Precision Engineering*, Vol. 17, 1995, pp. 211–221.

[13]Myrtle, T. F. and Friedmann, P. P., "Application of a New Compressible Time Domain Aerodynamic Model to Vibration Reduction in Helicopters Using an Actively Controlled Flap," *Journal of the American Helicopter Society*, Vol. 46, No. 1, January 2001, pp. 32–43.

[14]Patt, D., Liu, L., and Friedmann, P. P., "Simultaneous Vibration and Noise Reduction in Rotorcraft Using Aeroelastic Simulation," *Journal of the American Helicopter Society*, Vol. 51, No. 2, April 2006, pp. 127–140.

[15]Brentner, K., *A Computer Program Incorporating Realistic Blade Motions and Advanced Acoustic Formulation*, NASA Technical Memorandum, Vol. 87721 1986.

[16]Patt, D., Liu, L., Chandrasekar, J., Bernstein, D. S., and Friedmann, P. P., "Higher-Harmonic-Control Algorithm for Helicopter Vibration Reduction Revisited," *Journal of Guidance, Control, and Dynamics*, Vol. 28, No. 5, September-October 2005, pp. 918–930.